The Astrophysical Journal, 655:576–590, 2007 January 20
© 2007. The American Astronomical Society. All rights reserved. Printed in U.S.A.

A COMPREHENSIVE STUDY OF THE INITIATION AND EARLY EVOLUTION OF A CORONAL MASS EJECTION FROM ULTRAVIOLET AND WHITE-LIGHT DATA

A. Bemporad,[1] J. Raymond,[2] G. Poletto,[1] and M. Romoli[3]
Received 2006 July 5; accepted 2006 September 18

ABSTRACT

In this work we analyze simultaneous UV and white-light (WL) observations of a slow CME that occurred on 2000 January 31. Unlike most CMEs studied in the UV so far, this event was not associated with a flare or filament eruption. Based on vector magnetograph data and magnetic field models, we find that field disruption in an active region (AR) was driven by flux emergence and shearing motions, leading to the CME and to post-CME arcades seen in the EUV. WL images, acquired by the Mark IV coronagraph at the Mauna Loa Observatory, allowed us to identify the CME front, bubble, and core shortly (about 1 hr) after the CME ejection. From polarized brightness (*pB*) Mauna Loa data we estimated the mass and electron densities of the CME. The CME mass increases with time, indicating that about 2/3 of the mass originates above 1.6 $R_\odot$. Analysis of the UV spectra, acquired by the *Solar and Heliospheric Observatory* Ultraviolet Coronagraph Spectrometer (*SOHO* UVCS) at 1.6 and 1.9 $R_\odot$, allowed us to derive the electron temperature distribution across the CME. The temperature maximizes at the CME core and increases between 1.6 and 1.9 $R_\odot$. This event was unusual, in that the leading edge and the CME core were hotter than the ambient corona. We discuss magnetic heating and adiabatic compression as explanations for the high temperatures in the core and leading edge, respectively.

Subject headings: Sun: corona — Sun: coronal mass ejections (CMEs) — Sun: UV radiation

1. INTRODUCTION

A coronal mass ejection (CME) is a large structure of plasma and magnetic field that is expelled from the Sun into the heliosphere. In the last two decades these events have been widely studied, usually by white-light coronagraphs. However, a multiwavelength approach is needed because different phenomena in the chromosphere and the photosphere involved in the CME evolution give rise to emission in a broad wavelength interval that extends from radio to X-rays. CMEs may eject cool ($\sim 10^4$ K) chromospheric material, embedded in an erupting prominence, hot ($\sim 10^6$ K) coronal material, and flare plasma ($\sim 10^7$ K). During CME propagation, many processes may occur that interchange different forms of energy (kinetic, potential, electromagnetic, thermal, etc.), leading to plasma heating and cooling. The knowledge of plasma temperature and density within CMEs is important to understand these processes; however, at present their temperature structure heating rates are poorly known. First, from the observational point of view, CMEs appear in a large variety of geometric shapes, from the more typical three-part structure (an opening looplike bright front including a dark cavity or void and a bright core) to complex curved and twisted helical structures. It is at present unclear how much of the observed variety of CME geometries is a consequence of projection effects and how much is related to real differences in the physical structure of the CME source and/or of the background corona. It is often difficult to identify the plasma parameters of CME substructures superposed along the line of sight (LOS), and the three-dimensional geometry of CMEs is still debated, and this leads to uncertainties in the formulation of CME models. Second, CME models developed so far were aimed at reproducing only the CME white-light structure, which depends solely on the electron density distribution, while only a few attempts have been done to reproduce their UV appearance, which depends also on plasma temperature and outflow speed (see Ciaravella et al. 2001). This is probably due to the scarcity of simultaneous white-light and UV observations of CMEs. Most UV spectroscopic observations with good statistics are performed below the heliocentric distance of 2 $R_\odot$, while continuous 24 hr observations from space are available only above 2 $R_\odot$. As a consequence there are few simultaneous observations of CMEs in UV and white light at the same heliocentric distance focusing on the initiation and early evolution of CMEs (see Dere et al. 1997).

Nevertheless, in the last few years important information on the distribution of physical parameters within CMEs has been derived from the UV data acquired by the EUV Imaging Telescope (EIT; Delaboudinière et al. 1995) and the UVCS (Kohl et al. 1995) instruments on board the *SOHO* spacecraft. In particular, UVCS data make it possible to study (from the line Doppler shifts and the so-called Doppler dimming technique) the complex three-dimensional velocity structure of these events. Different CMEs show peculiar features at the core such as: a single bright emitting knot with transverse velocity changes (Ciaravella et al. 1999); many bright knots or spots with different velocities interpreted as "different, isolated CME structures" (Ventura et al. 2002); an *S*-shaped configuration suggesting a helical topology of the erupted prominence (Ciaravella et al. 2003); and rotation of the velocity vector associated with helical motion of plasma around "an erupted magnetic flux tube" (Antonucci et al. 1997). Often the CME core is visible in spectral lines from ions that form in a low-temperature plasma ($\sim 10^4$ K; see, e.g., Ciaravella et al. 1997; Ventura et al. 2002), but recent observations also detected higher temperature emission ($T > 1.6 \times 10^6$ K) in the CME void and at the top of the prominence core (Ciaravella et al. 2003). However, there are few studies on possible plasma heating sources within CMEs (see, e.g., Akmal et al. 2001).

In this work we describe the results obtained from the analysis of UVCS observations at 1.6 and 1.9 $R_\odot$ of a CME that occurred on 2000 January 31, and was simultaneously observed in white light with the Mark IV Coronagraph at the Mauna Loa Observatory.

[1] INAF–Osservatorio Astrofisico di Arcetri, Florence, Italy.
[2] Harvard-Smithsonian Center for Astrophysics, Cambridge, MA.
[3] Università di Firenze, Dipartimento di Astronomia e Scienza dello Spazio, Florence, Italy.

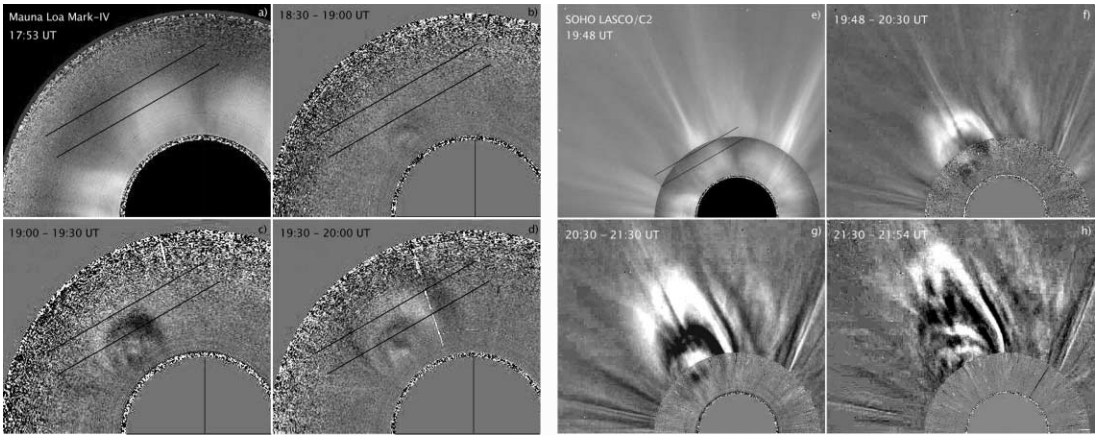

FIG. 1.—(*a*) Mauna Loa Mark IV image of the white-light corona in the first noncorrupted available image; for future reference, we plot here and in the following panels the position of the UVCS slit at 1.6 and 1.9 $R_\odot$ (see text). (*b–d*) Early phase of the 2000 January 31 CME development as seen by the Mauna Loa Mark IV Coronagraph. These images are constructed as differences between observations acquired at the times indicated in each panel: white color corresponds to a density increase, while black indicates a density decrease. (*e*) LASCO C2 image of the white-light corona before the CME front enters in the telescope field of view superposed onto a Mark IV image. (*f–h*) CME development observed in LASCO C2 and Mark IV difference images; in each panel we give times of LASCO images used to construct the differences.

Because our data cover the CME initiation in white light and UV at low altitudes ($\leq 2\ R_\odot$), we aim at inferring the physical parameters of the CME in its early stages. After a brief description of the event from white-light Large Angle and Spectrometric Coronagraph (LASCO) and Mauna Loa data (§ 2), we describe the evolution of the AR identified as the CME source as seen by *SOHO* EIT and the *Yohkoh* Soft X-Ray Telescope (SXT; Tsuneta et al. 1991) and by the Imaging Vector Magnetograph (IVM) at the Mees Solar Observatory (see Mickey et al. 1996) and *SOHO* Michelson Doppler Imager (MDI; Scherrer et al. 1995) instruments (§ 3). In §§ 4 and 5 we summarize, respectively, the UVCS and Mark IV observations. Then, after a brief description of the technique used in the white-light data analysis (§ 5.1), we derive the physical parameters of the three-part CME such as electron density (§ 5.2), CME mass (§ 5.3), and electron temperature (§ 6), while in § 7 we describe their evolution between 1.6 and 1.9 $R_\odot$. After a discussion of uncertainties possibly affecting our computations (§ 8), discussion and conclusions are given in § 9. We find that this CME differs from most of those studied so far in the UV, in that it originates rather high in the corona, and the leading edge and the core are hotter than the background corona. We discuss possible heating mechanisms and compare with CME theories.

2. THE 2000 JANUARY 31 CME: WHITE-LIGHT MORPHOLOGY

In this section we describe our event as seen by the *SOHO* LASCO and Mauna Loa/Mark IV coronagraphs.[4] The two LASCO C2 and C3 telescopes are externally occulted coronagraphs observing the white-light corona from 2.0 to 6.0 $R_\odot$ and from 3.7 to 32.0 $R_\odot$, respectively. LASCO data consist of a sequence of images taken typically every 24 minutes (for a more complete instrumental description, see Brueckner et al. [1995]). The Mark IV K-coronameter at the Mauna Loa Observatory acquires images of the low corona (700–1080 nm) from $\sim$1.12 to $\sim$2.79 $R_\odot$; data are acquired over a period of about 3 minutes with an angular resolution of 0.5°, and a 960×960 pixel image of the corona is then reconstructed.

[4] See Mauna Loa and LASCO movies at http://mlso.hao.ucar.edu/cgi-bin/mlso_datasum.cgi?2000&1&31&ACOS and http://lasco-www.nrl.navy.mil/daily_mpg/2000_01/, respectively.

The event occurred in the northeast quadrant. The LASCO C2 and C3 images show, late on 2000 January 31 ($\sim$18:30 UT), a complex of streamer-like features immersed in a diffuse brightness visible at all latitudes. In particular, three thin northward features are centered at latitudes of $\sim$N56°, N64°, and N78° (see Fig. 1*e*), respectively. Starting from the image acquired at 19:48 UT by LASCO C2 (previous frame at 18:54), a bright front appears centered at a latitude of $\sim$N58° (angular width of $\sim$50°; see Fig. 1*f*), followed by the arrival of a bright core (Fig. 1*g*). The CME propagates toward higher latitudes entering the LASCO C3 field of view near a latitude of $\sim$N65° and deflecting the northernmost radial feature westward. From the CME arrival times in the LASCO C2 and C3 field of view, the CME front propagates at a projected speed of $\sim$480 km s^{-1} at 3 $R_\odot$; hence, this event can be classified as a slow or gradual CME. Tracing the CME trajectory back in time we derive that it crosses the limb at a latitude of $\sim$N50°; this angle is used in § 3 for the identification of the CME source region.

Difference images from the Mauna Loa Mark IV coronameter show a complex system of rising looplike features that later reaches the LASCO C2 field of view generating the observed CME (see Figs. 1*b*–1*d*). In order to smooth the noise fluctuations we built these difference images from averages over about half an hour (i.e., 10 exposures). In Figure 2 (*left*) we show a Mark IV difference image (superposed for future reference onto an EIT Fe XII λ195 difference image) obtained from an average over 9 minutes, which is more representative of the "instantaneous" appearance of the CME. In this figure it is easy to recognize the opening CME front and the dark void; below the void the CME structure is more complex and shows looplike features surrounding a bright knot that we identify as the CME core. Vršnak et al. (2004) observed in Mark IV data an "oval" pattern surrounding the flux rope in the early phases of the CME and identified it as "the hot envelope formed by the reconnected field lines being wrapped around the rope." More recently an "helical structure surrounding the CME core" with the "shape of the flux rope surrounded by a bubble" has also been observed by Lin et al. (2005) in LASCO C2 images enhanced by the wavelet technique. Hence, in agreement with these authors, we interpret these features as the concentric loops at the edges of the CME bubble. Figures 1 and 2 also show that the UVCS slit (see below) is favorably located to observe the whole CME.

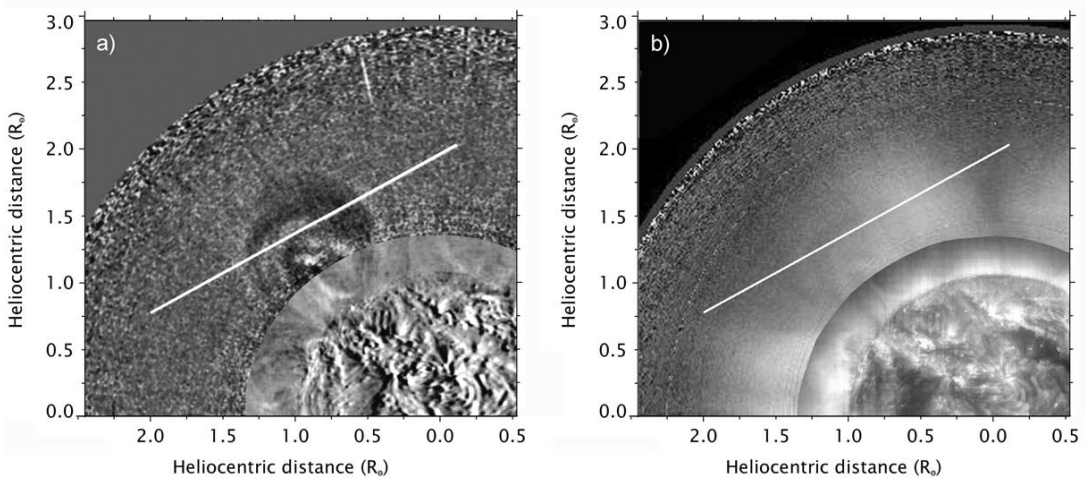

FIG. 2.—*Left*: Composite image obtained by superposing a Mauna Loa difference image (19:23–19:32 UT) and an EIT Fe XII difference image (18:36–19:25 UT) showing the CS connecting the neutral cusp-type *Y*-point (observed in the EIT field of view) and the expanding CME bubble (visible in the white-light image). *Right*: Corresponding nondifferenced images from Mauna Loa (19:23 UT) and EIT Fe XII (19:25 UT). For future reference, in both panels we also show the position of the UVCS slit at 1.6 $R_\odot$.

Because, as we describe in § 3, there are no clear signatures in the disk activity associated with our CME, the only estimate for the CME initiation time can be derived from white-light observations. However, CME start times inferred from LASCO images are only approximate. Figure 3 is a composite image showing the CME height versus time curve from the LASCO and Mark IV data obtained by integrating the observed intensity over 10° around the CME latitude (in order to exclude from the average the CME flanks) and subtracting the average pre-CME coronal intensity calculated over the whole data set. The resulting Figure 3 shows that the front seems to start rising at a heliocentric distance of about 1.6 $R_\odot$. From a second-order fit of the curve we find that the CME front starts rising (with zero initial speed) at ~18:13 UT[5] from a heliocentric distance of 1.52 ± 0.08 $R_\odot$ with an acceleration of 34 ± 4 m s^{-2}. This is more than 10 times larger than the acceleration derived from LASCO images at larger heights. These results are in agreement with studies of the CME main acceleration phase (see, e.g., Maričić et al. 2004) and in qualitative agreement with some CME models that predict the front material to be at a heliocentric distance ≤1.2 $R_\odot$ before it starts accelerating (see Lin et al. 2004).

As shown in Figure 3, the speed of the CME front increases from ~30 km s^{-1} at 1.6 $R_\odot$ (18:30 UT) up to ~160 km s^{-1} at 2.6 $R_\odot$ (20:00 UT), while the speed of the core shows a large spread of values between 70 and 100 km s^{-1}, but no significant acceleration. Hence, within the Mark IV field of view, the ratio between the front and core speed is no larger than 2. A similar ratio between the velocity of the CME front and its driver is acceptable and has been observed (see, e.g., Foley et al. 2003) and modeled (see, e.g., Chanè et al. 2005) by previous authors. However, Figure 3 shows that above ~2.5 $R_\odot$ the CME core starts to decelerate, while the front keeps accelerating. LASCO C2 images suggest that above this altitude the CME interacts with a preexisting radial structure (as suggested by the dark raylike feature that cuts through the CME front in Figs. 1*f* and 1*g*); this process leads to a destructuring of the whole CME three-part configuration (Fig. 1*h*) and probably disconnects the CME core from the expanding front. As a consequence in the LASCO C3 field of view, the CME appears as a "double event" with two unstructured expanding features. An analysis of this phenomenon is beyond the scope of this work, which concentrates on the CME early evolution. However, it is worth mentioning that in principle it is possible to interpret the whole event as consisting of two sequential CMEs. In this interpretation what we called "front" is the front of the first CME, while the looplike feature that we identified as the edges of the CME bubble surrounding the core are the front of the second CME. In our view the agreement of Figure 2 with previous observations of the CME three-part structure is a strong argument in favor of the single CME scenario.

[5] This time may correspond only to the initiation of the main acceleration phase; Mark IV data before this time show a streamer swelling that may indicate the real onset of the event to be at earlier times. Because we have no Mauna Loa observations before 17:30 UT (or before 17:42 UT, taking into account the poor quality of the first exposures), we cannot definitely infer the real CME start time.

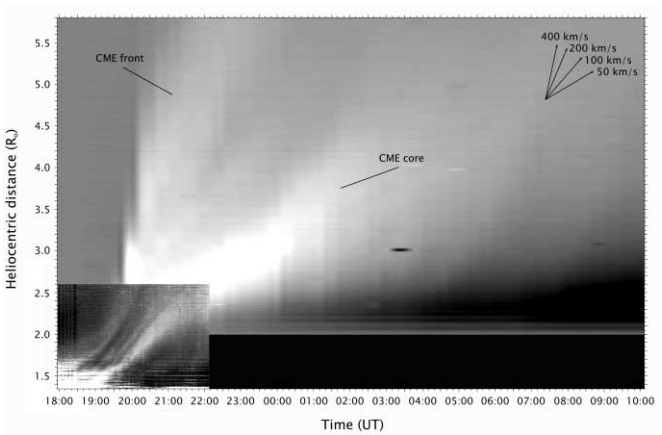

FIG. 3.—CME height vs. time image obtained by integrating over 10° around the CME latitude the Mauna Loa (*bottom left*) and LASCO C2 white-light images (see text).

3. PRE- AND POST-CME ACTIVITY

In this section, after the identification of the AR likely associated with our CME, we examine the available *SOHO* MDI, EIT, and *Yohkoh* SXT data with the aim of understanding what triggered the January 31 CME. The source region of the January 31 CME is not easily identified because the event was not associated with any flare and/or prominence eruption. On 2000 January 31 there are two ARs in the northeast quadrant (see Fig. 4): one of

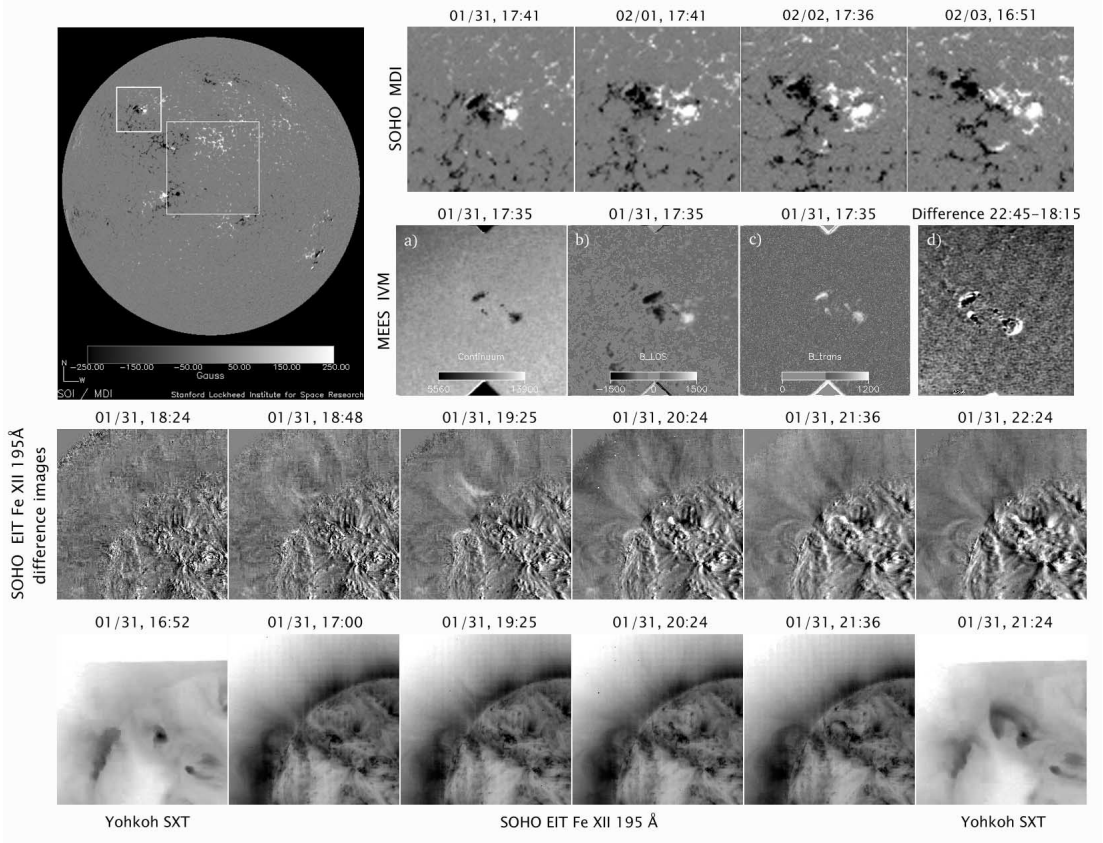

FIG. 4.—*Top left*: MDI image showing the position of AR 8851 in the northeast quadrant (*small white box*) less than 1 hr before our event. *First row*: Sequence of MDI images showing the progressive increase of the AR area and the relative motion of the two opposite polarities in the days after the event. *Second row*: (*a*) IVM white-light image of the two sunspots in the AR; the modulus of (*b*) the LOS and (*c*) the transverse magnetic field components; (*d*) a difference between two successive IVM white-light images showing the relative motion of the two sunspots. *Third row*: Sequence of EIT Fe XII images obtained by subtracting from each image, the last one acquired before the initiation of the eruption (17:48 UT); these images show the inflating EIT loops lying above the solar limb and the formation of the post-CME CS. *Fourth row*: Sequence of SXT and EIT images (in reversed color scale) showing the formation of the UV and X-ray post-CME arcades on the disk and the CS above the limb.

these two regions (NOAA 8852) is located too close to the solar center (N10°, E27° on 2000 January 31, 16:32 UT) to be the source of a CME that propagates mainly in the plane of the sky (see below). The second AR (NOAA 8851) is at N27°, E42° (see Fig. 4): the radial from this AR projects onto the plane of the sky at about N48°, hence, close to the latitude where the CME trajectory crossed the solar limb.

SOHO MDI observations show this region to be of a simple β-type magnetic morphology and to include a pair of sunspots and other satellite spots distributed along two parallel lines enclosing the magnetic neutral line (NL; see Fig. 4). The temporal evolution of AR 8851 shows a continuous increase in its area and identifiable sunspot number.[6] Also, images acquired by the IVM instrument at the Mees Observatory show that the two larger sunspots are moving in opposite directions and parallel to the magnetic neutral line.[7] These observations hint at flux emergence accompanied by shearing motions, both factors likely destabilizing the magnetic configuration above the AR (see, e.g., Liu et al. 2005).

In *SOHO* EIT Fe XII images before the event AR 8851 appears as a bright, small tunnel of loops connecting opposite polarities of the sunspot pair. EIT difference images made about 1 hr after the event (see Fig. 2) show a radial feature at the CME latitude connecting the neutral "*Y*" point and the white-light CME bubble. We consider this as evidence of the current sheet (CS) that forms above the EUV loops after the CME ejection disrupts the AR field. We note here that CSs have been identified in the wake of CMEs both in LASCO as thin, raylike features connected with the CME bubble (see, e.g., Webb et al. 2003; Lin et al. 2005) and by UVCS as emission from unusually high temperature ions (see, e.g., Ciaravella et al. 2002; Ko et al. 2003; Raymond et al. 2003; Bemporad et al. 2006); Figure 2 demonstrates that the CS structure can be observed also in EIT images. Figure 2 also shows that the extension at lower levels of the white-light opening looplike CME front connects with the opening branches observed in the EIT Fe XII images. A similar correspondence between the CME front and opening loops in the EIT field of view led Dere et al. (1997) to conclude that the front plasma was at a temperature higher than the surrounding corona; as we show in the next sections, the comparative analysis of the UVCS and Mark IV data confirms this result.

The magnetic field reconfiguration is also revealed in EIT Fe XII images by another expanding system of loops (developing after the event) whose westward footpoints connect AR 8851 with a region located $\sim 3^\circ$ northward and $\sim 16^\circ$ eastward (see Fig. 4). These loops become clearly visible in the EIT Fe XII images (Fig. 4) from the 21:24 UT frame, but brightenings at the two footpoints are already visible at about 19:00 UT. In the following hours these loops expand slowly outward, decreasing in intensity and finally disappearing on February 1. At the end of this section we

[6] See http://www.solarmonitor.org/region.php?date=20000201&region=08851.

[7] See http://www.solar.ifa.hawaii.edu/IVM/Movie/Quick/2000/ivm_AR8851_20000131.html.

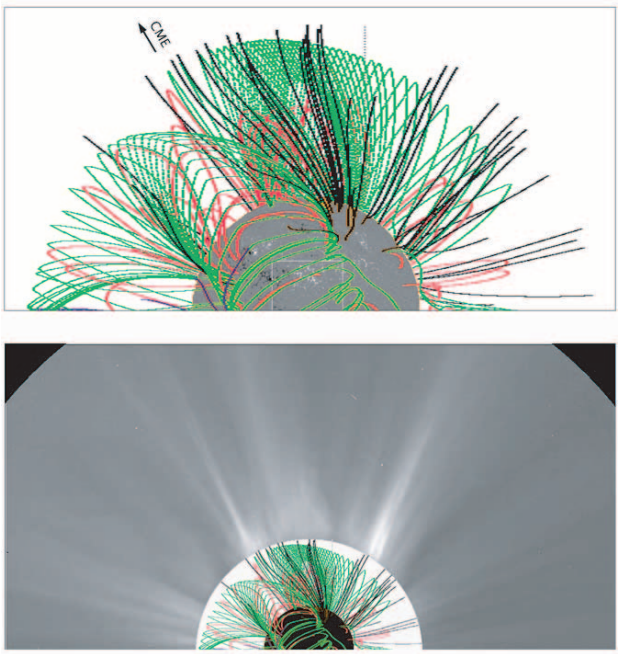

FIG. 5.—*Top*: Coronal magnetic field reconstructed from a PFSS (superposed onto an MDI image) starting from the photospheric fields measured during the Carrington rotation 1959. This image shows the streamer belts (*green*) and the close (*red*) and open (*black*) field lines; the black arrow marks the CME latitude. *Bottom*: Same as top, superposed onto the last LASCO C2 image acquired before the arrival of the CME front (19:48 UT).

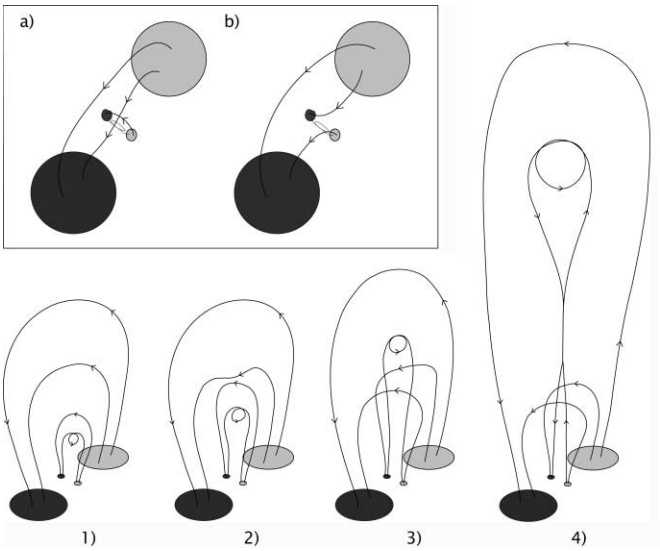

FIG. 6.—Cartoon showing a possible scenario for the CME occurrence. *Bottom row*: Magnetic shearing and flux emergence lead to the formation of a rising flux rope (1). Then, field lines connecting the opposite polarities (*dark gray*, negative; *light gray*, positive) of the sunspots interact with those connecting the external opposite polarity regions (2) leading to a magnetic reconnection that (3) leaves the flux rope free to escape. Then, during the following expansion, a CS forms below the CME bubble (4). *Top left*: Top view of the reconnection process occurring between phases (2) and (3).

interpret this secondary system of loops as a further consequence of the reconnection phenomena connected with the CME.

Activity in the AR is also observed by *Yohkoh* SXT. The observations have a gap of about 5 hr, around the time of the CME occurrence; however, when observations have been resumed (January 31, 21:24 UT; see Fig. 4), SXT images show a large X-ray-emitting arch whose footpoints roughly correspond to those of the secondary loop system seen in EIT Fe XII images. We conclude that a number of data from different experiments contribute to the identification of AR 8851 as the source of the January 31 CME. In our interpretation, the cusp-type loops observed above the solar limb in EIT Fe XII difference images are the "genuine" post-CME loops, while the EUV loops observed on the solar disk (Fig. 4) are probably a secondary product of the CME, as indicated by their asymmetric position with respect to AR 8851.

The CME was probably induced by the emergence of flux and by shearing motions in AR 8851 that lead to an unstable configuration, the formation of a flux rope, and eventually to the large-scale field disruption and CME ejection. In order to understand these processes and the origin of the helical flux ropes, it is important to study the interactions between the local ARs field and the large-scale ambient field, as has been recently done by several authors (see, e.g., Luhmann et al. 2003; Leamon et al. 2004). In particular, Luhmann et al. (2003) found that the presence of a bipolar AR below the streamer belt changes the global magnetic configuration and, depending on the tilt angle between the dipolar field and the source surface neutral line, may lead to a partial opening of some closed field lines. Hence, the emerging magnetic flux in newly formed ARs may induce significant topological changes in the coronal fields triggering the "breakout" opening of closed coronal field lines and, possibly, the ejection of mass along these lines (see, e.g., Liu et al. 2005).

In order to study the configuration of the coronal magnetic field above AR 8851 and provide a first-order representation of the large-scale magnetic field configuration we used the potential field source surface (PFSS; see, e.g., Altschuler & Newkirk 1969) model available at the Community Coordinated Modeling Center (CCMC) Web site[8] assuming a source surface radius of 2.5 $R_{\odot}$. Results from this model are given in Figure 5, which shows two groups of streamer belt field lines in the northeast quadrant. The first group crosses the solar disk in the northeast direction, then turns southward, and the second group projects over the solar limb in a high-latitude region (see green field lines in Fig. 5). An open field region (black field lines in Fig. 5) is also visible in EIT images as a darker region on the disk (Fig. 4). At lower altitudes, some closed field lines (red lines in Fig. 5) project onto the plane of the sky at the CME latitude, and other field lines connect the negative polarity region close to AR 8851 with a northward positive polarity region and indicate the connection between AR and background fields. If a flux rope was ejected from below these closed field lines nested within the streamer belts, these lines will expand toward the CME latitudes and possibly interact with the southern end of the polar streamer belts leading to the observed northward CME deflection.

We propose here a scenario for the CME occurrence and development, on the basis of the evidence described above. In the cartoon shown in Figure 6 we consider a small bipole (representing the sunspot pair magnetic field) embedded in the surrounding large-scale field (a positive and a negative unipolar region located northwest and southeast of the sunspot bipole, respectively; see MDI images in Fig. 4). According to MDI data, between the axes of the two nested bipolar fields there is an $\approx 90^{\circ}$ angle. The progressive twisting provided by the magnetic shearing (and shown by IVM data; see Fig. 4) and the corresponding change in the tilt angle between the AR bipolar field and the NL probably led to an unstable configuration and to the flux rope eruption ($\sim$18:00 UT; Fig. 6, panel 1). Because of the rising flux rope, magnetic reconnection occurs between the AR field and the overlying

[8] See http://ccmc.gsfc.nasa.gov/indexNavText.html.

large-scale field, leaving the flux rope free to escape (Fig. 6, panels 2–3, and from a top view, *a–b*). This "secondary" magnetic reconnection also leads to the formation of loops: these loops are those visible on the solar disk in *Yohkoh* SXT and *SOHO* EIT images (Fig. 4), which joins the positive and negative polarities of the sunspots with their eastward negative and westward positive spread out polarity regions, respectively. Below the expanding CME, a "primary" magnetic reconnection closes the open field, leading to the formation of the CS (Fig. 6, panel 4) observed above the solar limb in EIT difference images (Fig. 2); then the flux rope pushes the overlying closed field lines (red lines in Fig. 5) toward the coronal hole open field lines (black lines in Fig. 5). The material embedded in these arcades forms the CME front (which leaves the corona from a heliocentric distance of about 1.6 $R_\odot$; see Fig. 3), the flux rope forms the core, and the CME expands along the open field lines. Magnetic reconnection of field lines wrapped around the rising rope forms the white-light feature observed in between the CME front and the core (Fig. 2). During the expansion the CME interacts with the streamer belts above the north pole (Fig. 5), deflecting westward one of the radial structures visible in LASCO and being deflected northward as observed in LASCO images (Fig. 1).

4. UVCS OBSERVATIONS

The UVCS instrument (Kohl et al. 1995) on board the *SOHO* satellite consists of two channels for the observation of spectral lines in the UV range (namely, the O VI and Lyα channels) and one white-light channel. In this work we analyze data acquired by the O VI channel, which is optimized for observations in the spectral range around the O VI $\lambda\lambda$1031.90/1037.63 doublet and, at the selected grating position, covers the interval between 984 and 1080 Å in first order and 492–540 Å in second order. An additional mirror between the spectrometer grating and the detector allows observations at longer wavelengths that include the neutral hydrogen Lyα λ1215.67 line (redundant channel). The UVCS slit, perpendicular to the sunward direction on the plane of the sky, may be moved along the radial direction to observe the solar corona between 1.4 and 10 $R_\odot$ with a field of view of 40′, and it can be rotated by 360° around an axis pointing to the center of the Sun to cover all position angles. The detector pixel size corresponds to a spatial resolution of 7″ and a spectral resolution of 0.0993 Å (0.0915 Å pixel^{-1} for the redundant channel).

The UVCS observations of the January 31 CME started on 2000 January 31 at 17:05 UT and ended on February 1 at 02:00 UT. The UVCS slit was centered at a northern latitude of 60° in the east quadrant (see Fig. 1) at 1.6 and 1.9 $R_\odot$: the instrument took alternatively 12 exposures at 1.6 $R_\odot$ and three exposures at 1.9 $R_\odot$ (with an exposure time of 120 s); hence, we have nearly "simultaneous" observations of the same event at two different altitudes. The slit width was 50 μm: data were acquired with a spatial binning of 6 pixels (i.e., a spatial resolution of 42″) and a spectral binning of 1–3 pixels depending on the selected wavelength interval. In particular, the five selected spectral ranges are 1063.4–1068.1, 1029.5–1044.4, 1024.3–1027.7, 987.5–993.4, and 1211.8–1220.7 Å (redundant channel). Table 1 lists the lines included in these ranges, together with the temperature of formation of the emitting ion, from the ionization balance of Mazzotta et al. (1998).

Figure 7 (*top and bottom left panels*) shows the time evolution of the Lyα and O VI λ1032 line intensities at different latitudes along the UVCS slit centered at 1.6 $R_\odot$: in this section we report only results for this heliocentric distance, while data at 1.9 $R_\odot$ are discussed below (§ 7). It is difficult to identify in Figure 7 the passage of the CME: the data show only an approximately constant Lyα and O VI λ1032 line intensity until ~18:30 UT, then a rapid decrease (by about 30% and 40%, respectively), followed by some intensity fluctuations. Hence, we do not observe, as expected, a sharp rise in the line intensities at the time the CME front enters the UVCS slit. To enhance its visibility we show "running difference" UVCS images in the middle panels of Figure 7, which show that UVCS is imaging the expanding CME bubble. We surmise that the bright emitting knot imaged around 20:00 UT at a latitude of ≈50°–55° is the CME core, no longer visible at later times because it had already moved to higher levels. Around the core, the Lyα image shows the typical three-part structure of the CME, and the leading edge and dark void are also clearly visible. A similar structure is observable in the O VI running difference image, but the CME core is hardly visible. At later times, the Lyα CME image appears to be slightly "distorted" toward northward latitudes. This happens because, as already mentioned, the CME is deflected toward higher latitudes during observations. The CME structures are faint: for instance (Fig. 8, *left*) the core emission in the Lyα line is only ~10% higher than the background emission, while the O VI line enhancement is barely detectable and there is no emission from the Si XII line intensity (within a ~40% uncertainty; see Fig. 8, *right*).

TABLE 1
LINES INCLUDED IN THE UVCS SPECTRAL RANGES

λ_{obs} (Å)	λ_{ID} (Å)	Ion	Transition	log T_{max}
991.62.....	991.58	N III	$2s^2 2p^2 P_{3/2} - 2s 2p^2 {}^2D_{5/2}$	4.9
1025.69.....	1025.72	H I	Lyβ	4.5
1028.04.....	1028.04	Fe X	$3s^2 3p^4 3d^4 D_{7/2} - 3s^2 3p^4 3d^4 F_{7/2}$	6.0
1031.90.....	1031.91	O VI	$1s^2 2s^2 S_{1/2} - 1s^2 2p^2 P_{3/2}$	5.5
1034.50.....	1034.48	Ni XIV	$3s^2 3p^3 {}^4S_{3/2} - 3s^2 3p^3 {}^2P_{3/2}$	6.2
1036.34.....	1036.34	C II	$2s^2 2p^2 P_{1/2} - 2s 2p^2 {}^2S_{1/2}$	4.6
1037.02.....	1037.02	C II	$2s^2 2p^2 P_{3/2} - 2s 2p^2 {}^2S_{1/2}$	4.6
1037.63.....	1037.61	O VI	$1s^2 2s^2 S_{1/2} - 1s^2 2p^2 P_{1/2}$	5.5
1041.04.....	520.66	Si XII	$1s^2 2s^2 S_{1/2} - 1s^2 2p^2 P_{1/2}$	6.3
1215.67.....	1215.67	H I	Lyα	4.5
1219.58.....	609.79	Mg X	$1s^2 2s^2 S_{1/2} - 1s^2 2p^2 P_{3/2}$	6.8

In the selected spectral intervals there are neither two lines from different ionization states of the same element nor two different lines emitted from the same ion (see Table 1); hence, the line ratio techniques for the estimate of T_e (see, e.g., Wilhelm et al. 2002) cannot be applied. Moreover, the standard technique used to derive the electron density from the ratio between the O VI doublet lines (Noci et al. 1987) holds only for negligible outflows, which is not the case for CMEs. Hence, in order to infer the N_e-values, we use Mauna Loa *pB* measurements (as we describe in § 5).

5. MARK IV OBSERVATIONS

On 2000 January 31 the Mark IV K-coronameter at the Mauna Loa Observatory acquired 91 exposures from 17:30 to 22:07 UT; the first three exposures are corrupted and have not been used. The Mark IV *pB* measurements are shown in Figure 9; in order to facilitate the comparison, this figure (*left*) shows the *pB* measured at 1.6 $R_\odot$ over a rectangular area that matches the UVCS slit over the same timescale used for Figure 7. Faint structures are better visible in the right panel of this figure, where we show the difference images obtained after accumulating the original data over 9 minutes (three exposures). The *pB* is higher at positions along the slit that delineate branches, closely resembling the topology predicted by the Lin & Forbes (2000) model. The similarity between the *pB* and the Lyα images is not surprising: *pB*

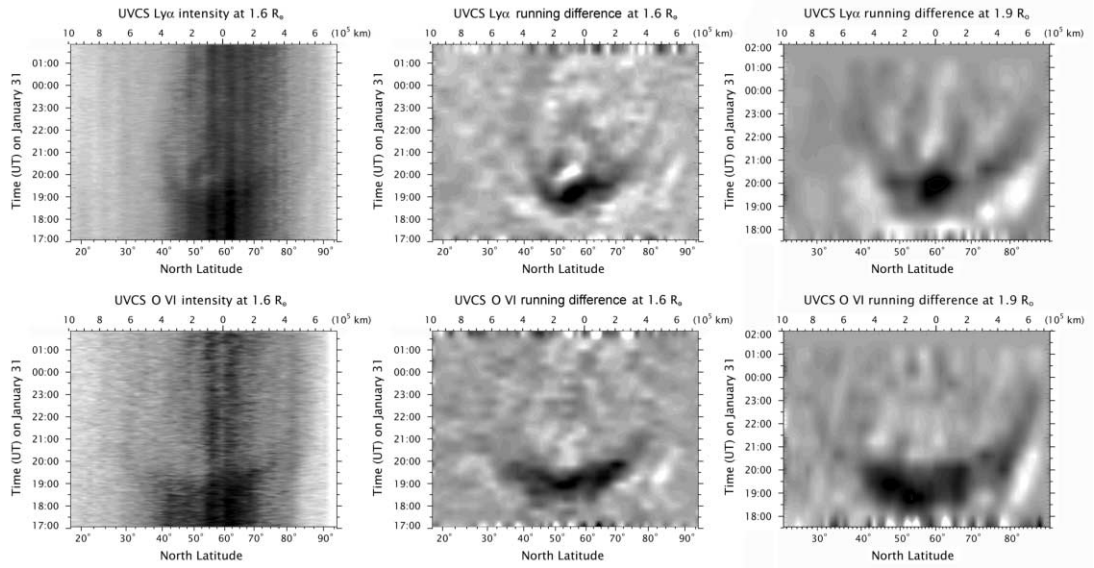

FIG. 7.—*Top left*: Lyα intensity evolution along the UVCS slit (*x*-axis) at different times (*y*-axis) as observed at 1.6 $R_\odot$. Colors range from 0 (*white*) to 5.2×10^{11} photons cm^{-2} s^{-1} sr^{-1} (*black*). *Top center*: Lyα running difference evolution at 1.6 $R_\odot$, colors from -4×10^{10} (*black*) to $+3 \times 10^{10}$ photons cm^{-2} s^{-1} sr^{-1} (*white*). *Bottom left*: Same as top left, for the O VI λ1032 line, colors from 0 (*white*) to 3.1×10^{11} photons cm^{-2} s^{-1} sr^{-1} (*black*). *Bottom center*: Same as top center, for the O VI λ1032 line, colors from -3×10^{9} (*black*) to $+3 \times 10^{9}$ photons cm^{-2} s^{-1} sr^{-1} (*white*). *Top and bottom right*: Same as top and bottom center, for data acquired at 1.9 $R_\odot$.

depends on the electron density, and, for a fixed outward velocity and approximately constant electron temperature, the Lyα intensity is dictated by the electron density as well.

Both *pB* (Fig. 9, *left*) and UVCS (Fig. 7, *left*) data show, until $\approx$18:30 UT, a bright emission that disappears after $\sim$19:00 UT. As shown in Figure 3, the CME front seems to start rising at a heliocentric distance of about 1.5–1.6 $R_\odot$ (i.e., about the height of the UVCS slit). This may explain why we do not see the arrival of the CME front onto the UVCS slit (i.e., a sudden increase in the line intensities) and we see only an intensity decrease preceding the arrival of the CME core: at the beginning of our observations the front material is probably "in equilibrium" at the height of the UVCS slit. Hence, this material is ejected outward, and we see an intensity decrease because of the plasma electron density decrease at this height.

In §§ 5.1 and 5.2 we use the Mark IV *pB* data to evaluate the CME electron density N_e. Then, given the outflow speed $v_{\rm out}$, we estimate T_e from a comparison of the predicted and observed UV line intensities in the CME core, front, and void (§ 6). From the density measurements we also estimate the mass of different CME features (§ 5.3).

5.1. *Density Diagnostics from White-Light Observations*

The observed $pB(\rho)_{\rm obs}$ as a function of the distance of observation ρ is given by an integral along the LOS, $z = (r^2 - \rho^2)^{1/2}$, of a geometric function (see Altschuler & Perry 1972) multiplied by the local density $N_e(z)$, the total Thompson cross section $\sigma_{\rm T}$ and other constant factors. The $pB(\rho)_{\rm obs}$ profile can be inverted (by assuming the density to be expressed in powers of the heliocentric distance r) via the van de Hulst technique (van de Hulst 1950) and an electron density profile $N_e(r)_{pB}$ can be derived.

Given the uncertainties of the Mark IV instrument (see Elmore et al. 2003), we have reliable *pB*-values only below $\sim$2 $R_\odot$ (see left panel in Fig. 10); hence, the $N_e(r)_{pB}$ profile derived with the above technique gives reliable density values only at heliocentric distances lower than this altitude. As we discuss below (§ 6),

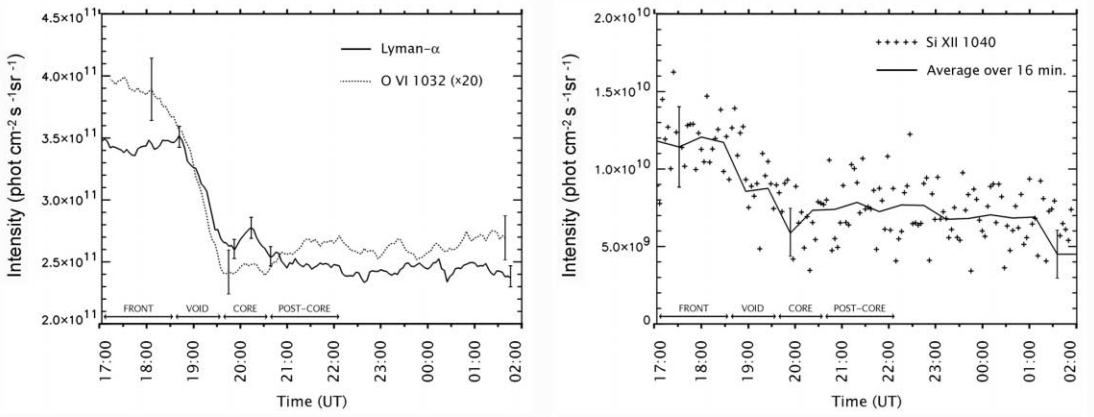

FIG. 8.—*Left*: Lyα and O VI λ1032 intensity evolution averaged over 10° around a latitude of N50°. Note that both spectral lines show an intensity decrease (which corresponds to the transit of the CME void), but only the Lyα line has a significant emission at the CME core (around $\sim$20:00 UT); this is interpreted as a combination of temperature and Doppler dimming effects (see text). *Right*: Time evolution of the Si XII λ1040 line (*plus signs*) and its average over 16 minutes (*solid line*), showing possibly a minimum at the time of the CME core transit.

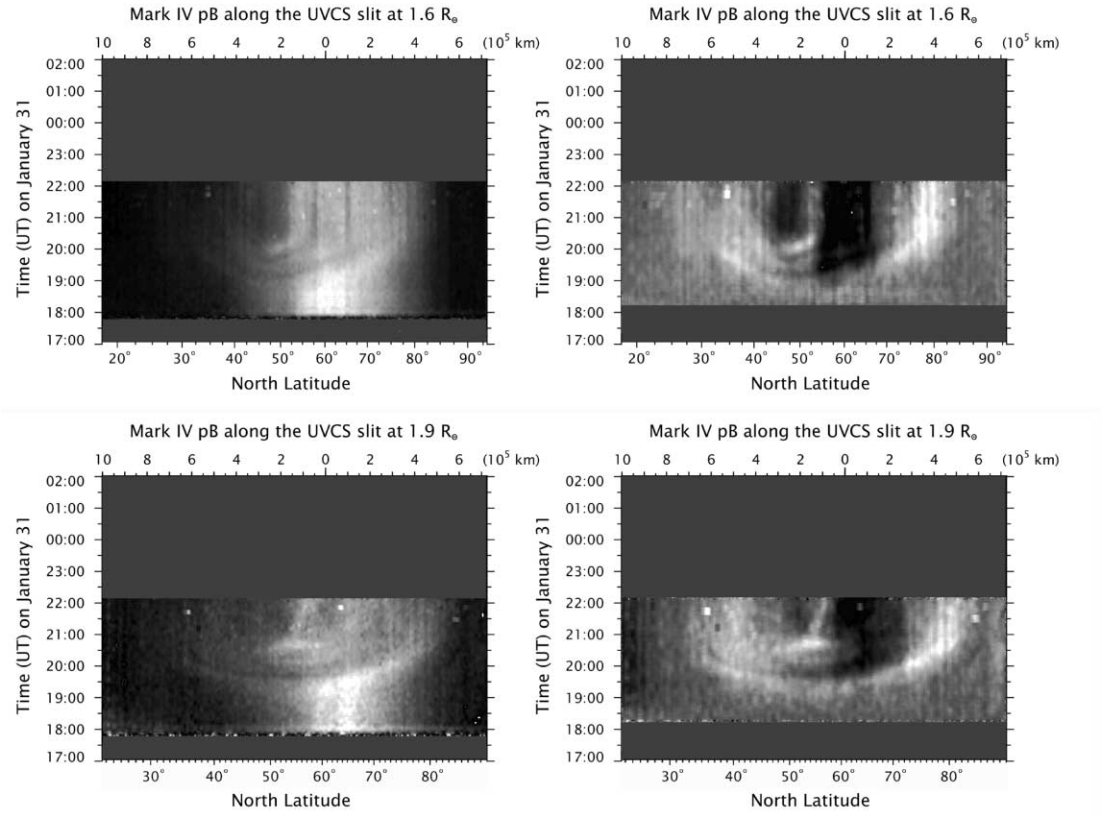

FIG. 9.—*Top left*: Mauna Loa Mark IV *pB* as measured at the position of the UVCS slit at 1.6 $R_\odot$ (*x*-axis) at different times (*y*-axis). To facilitate a comparison between Mark IV *pB* and Lyα images (see Fig. 7), *pB* data have been plotted on the same scale as the UVCS data; colors range from 0 to 8×10^{-8} (in units of $B_\odot^{-1}$). *Top right*: Same as top left, but with the difference image at 1.6 $R_\odot$ obtained by subtracting the average *pB* over the first ~30 minutes from the following exposures. *Bottom left and bottom right*: Same as top left and top right, at 1.9 $R_\odot$.

in order to derive the CME plasma electron temperature from the UV line intensities we also need to estimate the contribution to the observed emission originating from the corona behind and in front of the CME along the LOS. For instance, 90% of the observed Lyα coronal emission along the LOS at 1.9 $R_\odot$ arises from a region centered on the plane of the sky about 6 $R_\odot$ thick. This implies that for our UV data analysis we need a density profile reliable at least up to a heliocentric distance of ~3.5 $R_\odot$.

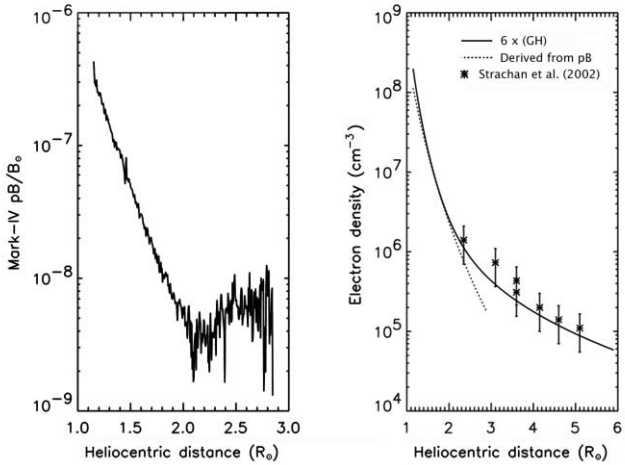

FIG. 10.—*Left*: Mark IV observed radial *pB* profile (17:42 UT) averaged over 10° around a latitude of N50°. *Right*: Comparison between the density profile derived via *pB* inversion (*dotted line*), the GH profile multiplied by a factor of 6 (*solid line*), and densities derived from the LASCO *pB* observed in a coronal streamer (Strachan et al. 2002, *stars*).

The above considerations led us to use the following method to evaluate an $N_e(r)$ profile representative of the coronal background electron densities before the arrival of the CME. First, analyzing the available *pB* coronal images at the CME latitude immediately before the event, we found from the *pB* inversion technique that the electron density below ~2 $R_\odot$ is given by $N_e(r)_{pB} = 3 \times 10^8/r(R_\odot)^7$ (cm^{-3}). Above that height we assume the Guhathakurta & Holzer (1994, hereafter GH) profile $N_e(r)_{\rm GH}$, which is given by

$$N_e(r)_{\rm GH} = (1.4 \times 10^6) r^{-2.8} + (8.0 \times 10^7) r^{-8.45} + (8.1 \times 10^7) r^{-16.87}, \quad (1)$$

times the constant multiplier k required to make $N_e(r)_{\rm GH} = N_e(r)_{pB}$ for heliocentric distances ≤ 2 $R_\odot$. Because the Thompson scattering is more efficient when the photon scattering angle is 90°, the main contribution to $pB(\rho)_{\rm obs}$ arises from the coronal plasma close to the plane of the sky (i.e., z smaller than ~1 $R_\odot$ from this plane). As a consequence, the main differences between the pre-CME and the CME *pB* observed values are due to changes in the electron density in a region close to this plane. Moreover, the January 31 CME appears to propagate mainly in the plane of the sky (as confirmed also by the absence of Doppler shifts in the UV spectral lines; see below). Hence, we evaluate N_e in transient coronal structures under the assumption that the electron density profile along the LOS is

$$N_e(z) = kN_e(z)_{\rm GH}, \quad \text{if } |z| > L/2,$$
$$N_e(z) = kN_e(z)_{\rm GH} + \bar{N}_e, \quad \text{if } |z| \leq L/2, \quad (2)$$

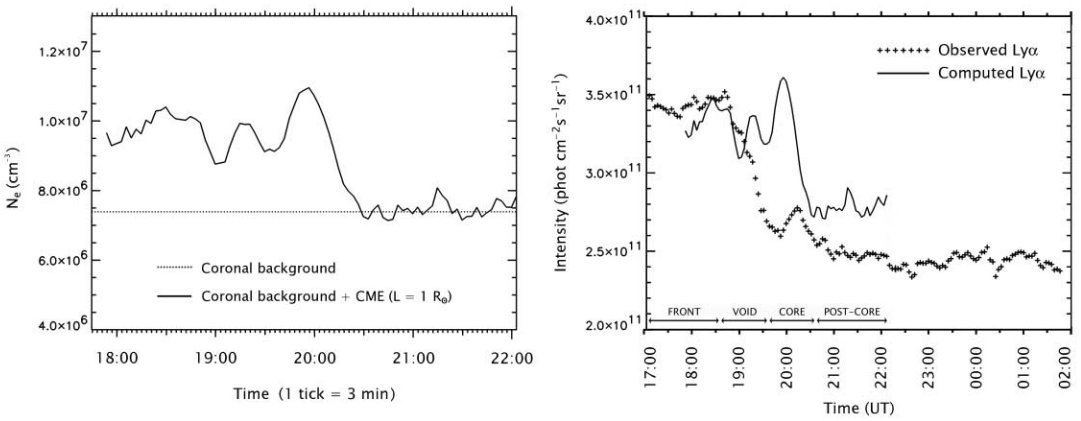

FIG. 11.—*Left*: Background plus additional electron density (*solid line*) as computed (assuming a CME extension L along the LOS of 1 $R_\odot$) from the Mark IV *pB* data as a function of time averaged over 10° around a latitude of N50°. Values of the additional density $\bar{N}_e$ (see text) can be obtained by subtracting from the solid curve the background constant density of 7.4×10^6 cm^{-3} (*dotted line*). *Right*: Comparison between the evolution of the observed Lyα intensity (*plus signs*) and the Lyα intensity computed from the densities shown on the left, for negligible outflows and a plasma temperature $T_e = 10^{6.2}$ K (see text).

where $\bar{N}_e$ is the additional electron density that allows us to reproduce the observed *pB*. The length L is a free parameter that can be evaluated from the dimension projected onto the plane of the sky of the considered structure assuming an a priori three-dimensional geometry. The additional density $\bar{N}_e$ is, in first approximation, inversely proportional to L, so that the product $\bar{N}_e L$ is nearly independent of the choice of L. This method yields an average electron density $\langle N_e \rangle$ in the region given by

$$\langle N_e \rangle = \frac{1}{L} \int_{-L/2}^{+L/2} \left[k N_e(z)_{\rm GH} + \bar{N}_e \right] dz. \qquad (3)$$

We note that the observed *pB* depends solely on the distribution of N_e along the LOS, unlike the UV line intensities, which also depend on the outflow speed $v_{\rm out}$ and the electron temperature T_e. Therefore, no further assumptions are needed about the plasma physical parameters. This gives us a means to disentangle N_e and T_e from $v_{\rm out}$ in the observed UV intensities. In the next sections we describe the results of this analysis, and in § 8 we discuss how possible variations in the N_e distribution we assumed along the LOS may affect our results.

5.2. *Estimate of the CME Electron Density*

The procedure described in the last section has been applied pixel by pixel (along the UVCS slit) to the region occupied by the CME, throughout the time interval covered by our observations. Before describing the results, we qualitatively discuss what can be inferred from observations. As we have shown in Figure 9, *pB* data reveal the bright CME core, so we expect the core plasma to be denser than the surrounding regions. However, after the transit of the CME front, the Lyα, O VI, and Si XII line intensities decrease, and significant emission from the core is seen only in the Lyα line (see Fig. 8). The radiative component of the O VI line can be reduced by Doppler dimming, but its collisional component and the intensity of the Si XII line can be reduced (in spite of an increase in electron density) only by temperature effects. In particular, because the O VI and Si XII emissivities peak at temperatures of $\log T = 5.5$ and 6.3, respectively (in this work we used the line emissivities given by the CHIANTI spectral code, ver. 5, with the ionization balance of Mazzotta et al. [1998]), a decrease of the collisional component of both lines can be explained only by a temperature increase above $\log T = 6.3$; hence, we may expect the core region to be denser and hotter than the surrounding plasma.[9] In the following we show how this qualitative conclusion is confirmed by our quantitative analysis.

In Figure 11 (*left*) we show the results from the technique described in the last section; in particular, in this figure we give the coronal background electron density and the additional density $\bar{N}_e$ at the latitudes of the CME core as a function of time. By comparing this plot with the top panels in Figure 9 it is possible to identify clearly the transit at the UVCS slit height of the CME front (between 18:00 and ~18:50 UT) and core (density peak around 20:00 UT); this is also confirmed by the Lyα evolution shown in Figure 8 (*left*). In between the front and the core, the density plot of Figure 11 (*left*) shows a secondary peak (~19:20 UT): this is the CME substructure that, in § 2, we identified as the edges of the CME bubble also visible in Figure 2. This substructure gives no significant emission in the UV lines: the left panel of Figure 8 shows between the CME front and the core only a decrease in the Lyα and O VI line intensities. Hence, in the following we refer to this region simply as to the CME "void": we warn the reader that the density value we derived in the void has to be considered an upper limit to the void density, because of the presence of CME substructures in the same region.

The background *pB* has been reproduced by multiplying the GH density profile by a factor of $k = 6$ (see eq. [2]). Figure 10 (*right*) shows that the so obtained profile is in good agreement below ~2 $R_\odot$ with the profile derived from the Mark IV observed *pB* and above this altitude with previous measurements (Strachan et al. 2002) in a coronal streamer. The CME density has been derived by assuming an increased density $\bar{N}_e$ over an extension along the LOS $L = 1$ $R_\odot$ centered on the plane of the sky. This assumption has been suggested by the average dimension projected onto the plane of the sky of the CME bubble (see Fig. 9), which apparently moves on that plane because we do not observe any significant line Doppler shift. The computed $\bar{N}_e$-values strongly depend on the selected L-values; however, the average Lyα emission is not significantly affected. In coronal plasmas the Lyα emission, due mainly to the radiative excitation, is roughly proportional to the factor $N_e L$. Because a decrease in L is balanced by an increase in the $\bar{N}_e$ computed from the observed *pB* and vice versa, the assumption of the L-value does not significantly

[9] The O VI intensity decrease could also be explained by a temperature decrease below $\log T = 5.5$, but in this case we should observe a Lyα intensity much larger than observed.

affect the computed Lyα line intensity (uncertainties in this technique are discussed in § 8). The right panel of Figure 11 compares the observed Lyα intensity and the intensity computed from the *pB*-derived densities shown in the left panel of the same figure: this plot is discussed in § 6. We anticipate that the lack of agreement between the observed and reconstructed Lyα intensities in this figure will be ascribed to the evolution of plasma parameters throughout the CME (§ 6).

5.3. *Estimate of the CME Mass*

The CME mass is derived from the observed *pB* by converting the excess brightness images to excess mass images. This is done by "assuming three factors: the CME depth and density distribution along the line of sight and the angular distance of the CME from the plane of the sky" (Vourlidas et al. 2000). These are the same assumptions we made in our computation of the electron density; hence, the two techniques are analogous. According to our previous computations, in this section we estimate the mass of the different parts of the CME by assuming that the additional electron density $\bar{N}_e$ derived from the *pB* data is representative of the CME density. Because the CME three-dimensional geometry is unknown, the derived values will give only an approximate estimate of the real CME mass and depend on the assumed geometry.

From Figures 7 and 9 we see that (projected onto the plane of the sky) the bright CME core has a typical radius of order $r_{\rm core} \simeq 0.1\ R_\odot \simeq 1.4 \times 10^5$ km. In order to infer the mass of the core we assumed either (1) a high-density spherical blob of plasma with radius $r_{\rm core}$ or (2) a cylindrical structure with base surface $\pi r_{\rm core}^2$ extending over a depth of 1 $R_\odot$ along the LOS and crossing the plane of the sky. In spherical geometry the core extends along the LOS over 0.2 $R_\odot$, and the additional electron density $\bar{N}_e$ we computed to reproduce the observed *pB* is about 5 times larger than the density previously computed (Fig. 11), so that the product $N_e L$ keeps approximately constant; in this geometry we estimate a core mass of $\sim 3 \times 10^{13}$ g. In cylindrical geometry ($L = 1\ R_\odot$) the additional density is of order $\bar{N}_e = 3.5 \times 10^6$ cm^{-3} (see Fig. 11 and Table 2), and the core turns out to have a mass of $\sim 6 \times 10^{13}$ g.

In order to derive the mass of the CME front we assumed either (1) a hemispherical shell surrounding the core with thickness and internal radius of 2×10^5 km or (2) a semicylindrical sheath with thickness and internal radius of 2×10^5 km extending along the LOS over 1 $R_\odot$ (see Figs. 7 and 9). Starting from an additional density $\bar{N}_e \simeq 2.7 \times 10^6$ cm^{-3} (see Fig. 11 and Table 2), the front mass in the two geometries turns out to be (1) $\sim 5 \times 10^{14}$ g or (2) $\sim 6 \times 10^{14}$ g, respectively.

As for the CME void between the front and the core, by assuming the shape of a hemispherical shell with internal radius of 1.4×10^5 km and thickness of 6×10^4 km, with an additional density of 2×10^6 cm^{-3} we derive a mass of $\sim 7 \times 10^{13}$ g, while with a semicylindrical sheath with the same thickness extending along the LOS over 1 $R_\odot$ the mass turns out to be $\sim 1 \times 10^{14}$ g. However, as already mentioned, because of the presence of the secondary substructures between the CME front and core, the estimated void density (and hence its mass) has to be considered as an upper limit.

In conclusion, the total CME mass we estimate is of order $(6\text{–}8) \times 10^{14}$ g depending on the adopted geometry; this mass resides mostly in the CME front surrounding the core, while the mass of the core is less than 10% of the total CME mass.

6. UVCS DATA: ESTIMATE OF THE CME ELECTRON TEMPERATURE

Given an a priori *L*-value and the electron density N_e and plasma outflow speed $v_{\rm out}$ (hence the Doppler dimming factors for the Lyα and O VI lines), we may compute the expected Lyα, O VI, and Si XII line intensities as a function of T_e: a comparison of the predicted and the observed intensities allows us to infer the electron temperature of the plasma. However, the Si XII is a second-order line and, because of the large uncertainties in the estimate of its intensity (see Fig. 8, *right*), cannot be used to infer temperatures, while the Lyα and O VI line intensities have a better signal-to-noise ratio. Both these spectral lines may have a radiative and a collisional component; however, at typical coronal temperatures ($T \sim 10^6$ K), collisional excitation would give a ratio between the Lyβ and Lyα intensities of order $\sim$0.13–0.14, while for resonant scattering a much lower ratio ($\sim$0.001–0.002) is expected (see, e.g., Raymond et al. 1998). Because in our data the observed $I(\mathrm{Ly}\beta)/I(\mathrm{Ly}\alpha)$ ratio is of order $\sim$0.004 and $\sim$0.002 at the beginning and at the end of UVCS observations, respectively, we can safely assume that the observed Lyα emission arises almost entirely from radiative excitation, making it easier to estimate the expected Lyα intensity $I_{\rm exp}(\mathrm{Ly}\alpha)$. Moreover, possible uncertainties in the $v_{\rm out}$ values do not sensibly affect the computed $I_{\rm exp}(\mathrm{Ly}\alpha)$ for $v_{\rm out} \leq 100$ km s^{-1} (see, e.g., Kohl et al. 1997). Hence, the computation of the Lyα intensity is easier than that of the O VI line, for which we have to compute both the radiative and collisional components and the estimate of the Doppler dimming factor is more critical. For these reasons we infer temperatures from the Lyα intensity, while we use the O VI and Si XII line intensities for a consistency check.

In order to compare the observed line emissions with those computed from the CME region, we need to evaluate the contribution from the external corona behind and in front of it along the LOS. To this end, it is necessary to assume a background density profile, electron temperatures, outflow speeds, and disk intensities. In agreement with our previous computation, we used the N_e profile discussed in § 5.1 (eq. [2]). Moreover, we assumed the electron temperature to be constant along the LOS and equal

TABLE 2

Lyα, O VI λ1032, AND Si XII λ1040 LINE INTENSITIES AT 1.6 $R_\odot$

CME Region	Front	Void	Core	Postcore
Observed Line Intensities (photons cm^{-2} s^{-1} sr^{-1})				
I(Lyα) (10^{11})	3.5 ± 0.1	2.6 ± 0.1	2.8 ± 0.1	2.5 ± 0.1
I(O VI λ1032) (10^{10})	1.9 ± 0.1	1.2 ± 0.1	1.2 ± 0.1	1.2 ± 0.1
I(Si XII λ1040) (10^{10})	1.2 ± 0.2	0.8 ± 0.1	0.7 ± 0.1	0.8 ± 0.1
Computed Line Intensities (photons cm^{-2} s^{-1} sr^{-1})				
$I(\mathrm{Ly}\alpha)^{\rm CME}$	1.8×10^{11}	1.1×10^{11}	1.2×10^{11}	9.5×10^{10}
$I(\mathrm{Ly}\alpha)^{\rm TOT}$	3.4×10^{11}	2.7×10^{11}	2.8×10^{11}	2.6×10^{11}
$I(\mathrm{O\ VI}\ \lambda1032)^{\rm CME}_{\rm rad}$	3.8×10^9	2.0×10^9	6.0×10^8	7.6×10^8
$I(\mathrm{O\ VI}\ \lambda1032)^{\rm CME}_{\rm col}$	7.2×10^9	2.7×10^9	1.9×10^9	1.7×10^9
$I(\mathrm{O\ VI}\ \lambda1032)^{\rm CME}_{\rm tot}$	1.1×10^{10}	4.7×10^9	2.5×10^9	2.5×10^9
$I(\mathrm{O\ VI}\ \lambda1032)^{\rm TOT}$	1.9×10^{10}	1.2×10^{10}	1.0×10^{10}	1.0×10^{10}
$I(\mathrm{Si\ XII}\ \lambda520)^{\rm CME}$	8.4×10^9	6.5×10^9	4.7×10^9	3.9×10^9
$I(\mathrm{Si\ XII}\ \lambda520)^{\rm TOT}$	1.0×10^{10}	9.0×10^9	7.0×10^9	6.0×10^9
Plasma Parameters				
N_e (cm^{-3})	1.0×10^7	9.4×10^6	1.1×10^7	7.4×10^6
$\log T_e$	6.30	6.40	6.45	6.40
$v_{\rm out}$ (km s^{-1})	30	50	80	80

NOTES.—Lyα, O VI λ1032, and Si XII λ1040 line intensities observed and computed in the CME front, void, core, and postcore (see text) at 1.6 $R_\odot$. For a discussion of the uncertainties in the computed values, see § 8.

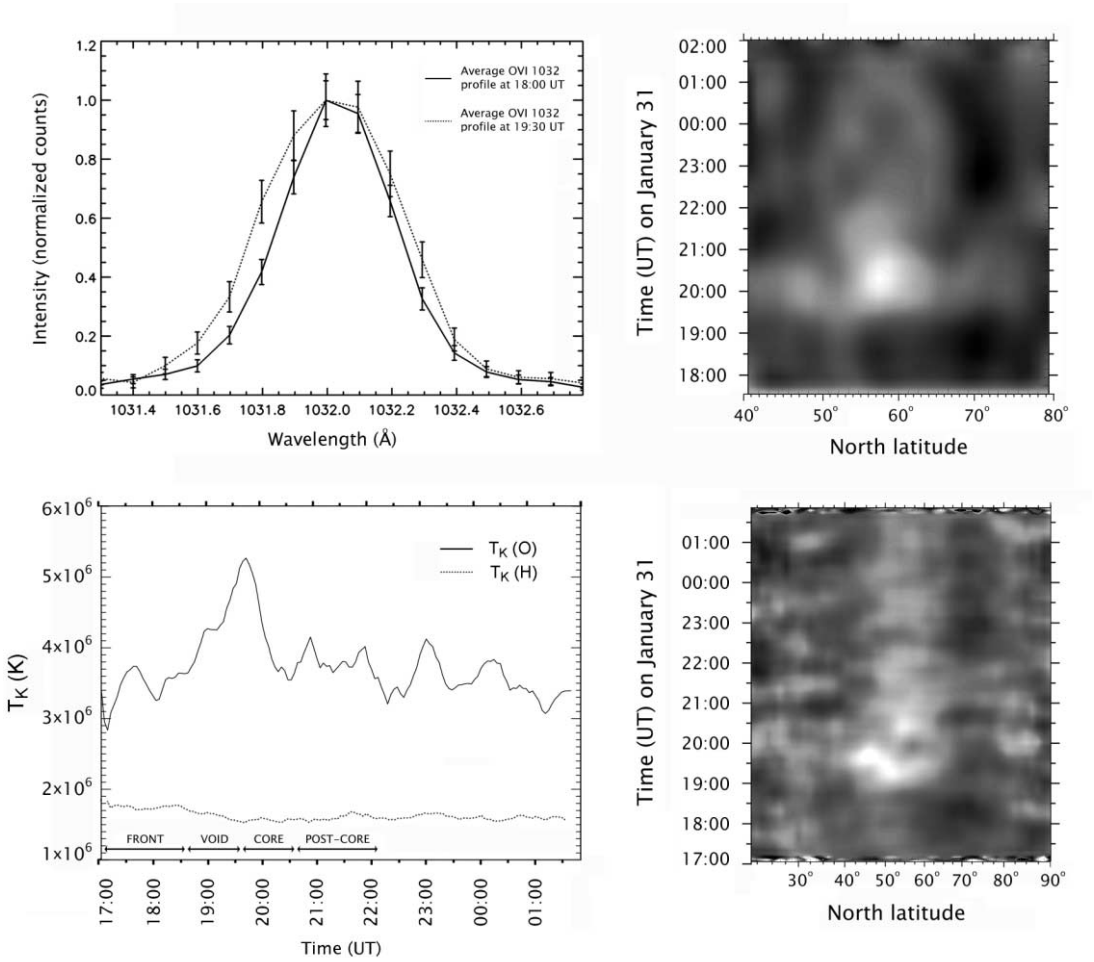

FIG. 12.—*Top left*: Comparison between the normalized O VI λ1032 line profiles at two different times (averaged over four spatial bins around the latitude of $\simeq$N50° and four exposures) showing a $\sim$25% line broadening (FWHM) at an intermediate position between the CME void and core. *Bottom left*: Evolution at the CME latitude of the hydrogen (*dashed line*) and oxygen (*solid line*) kinetic temperatures as derived from Gaussian fits of the O VI λ1032 and Lyα line profiles. *Bottom right*: Evolution along the UVCS slit (i.e., at different latitudes) of the oxygen kinetic temperatures; colors range from 3 (*black*) to 5×10^6 K (*white*). *Top right*: Same as bottom right, for data acquired at 1.9 $R_\odot$; colors range from 2 (*black*) to 5×10^6 K (*white*).

to the kinetic temperature of $10^{6.20}$ we derived from Gaussian fits to the Lyα line profile (see below), the outflow speed $v_{\rm out}$ to be $\approx$100 km s^{-1} constant along the LOS, and the disk intensities to be equal to the values we estimated for the 2000 June observations (see Bemporad et al. 2003). We then assumed that the measured intensities derive from a background coronal emission plus a CME emission, originating from a region centered on the plane of the sky and (in agreement with the analysis we performed on *pB* data) extending over a length $L = 1\ R_\odot$ along the LOS. The Lyα, O VI λ1032, and Si XII λ1040 line intensities from the background corona at 1.6 $R_\odot$ turn out to be 1.6×10^{11}, 7.7×10^9, and 2.0×10^9 photons cm^{-2} s^{-1} sr^{-1}, respectively. These values have to be added as a constant background to the line intensities estimated for the CME region in order to reproduce the observed intensities.

We started our computations at the CME front: in this region, by assuming an outflow speed of $\sim$30 km s^{-1} (as suggested by the Mauna Loa *pB* observations; see Fig. 3) and by using values for the fraction of neutral hydrogen atoms as a function of temperature given by the CHIANTI spectral code (ver. 5.0) with the ionization equilibrium of Mazzotta et al. (1998), the observed Lyα intensity of 3.5×10^{11} photons cm^{-2} s^{-1} sr^{-1} is reproduced provided the average electron temperature in the CME region is $\log T_e = 6.3$. At later times, the right panel of Figure 11 shows that the Lyα intensities computed from the electron densities we derived, assuming the same temperature and outflow speed we assumed in the CME front, are significantly different from the observed values. Hence, it is necessary to assume different values of T_e and $v_{\rm out}$ in order to reproduce the intensities observed at later times. Taking advantage of the outflow speeds measured from Mauna Loa data, we infer the electron temperature we need to reproduce the observed Lyα intensities after the transit of the CME front.

Results from this computation are given in Table 2; the outflow speed in the CME void is assumed to be intermediate between the front and core speeds (see Fig. 3). For the postcore the value is uncertain because there are no visible *pB* structures in the region, and we assumed the same speed as that of the CME core. In this table, errors in the observed intensities are of order 2%, 5%, and 18% for Lyα, O VI, and Si XII intensities, respectively, starting from $\sim$20:00 UT throughout the whole data set, while we derived slightly smaller errors at earlier times when line intensities are larger. Regions in the first row of Table 2 correspond to the segments shown in Figure 11 (*right*); these also show the time intervals over which we computed the average observed intensities and plasma parameters given in Table 2. Once the Lyα intensities have been reproduced with the appropriate plasma temperatures, we computed as a consistency check the

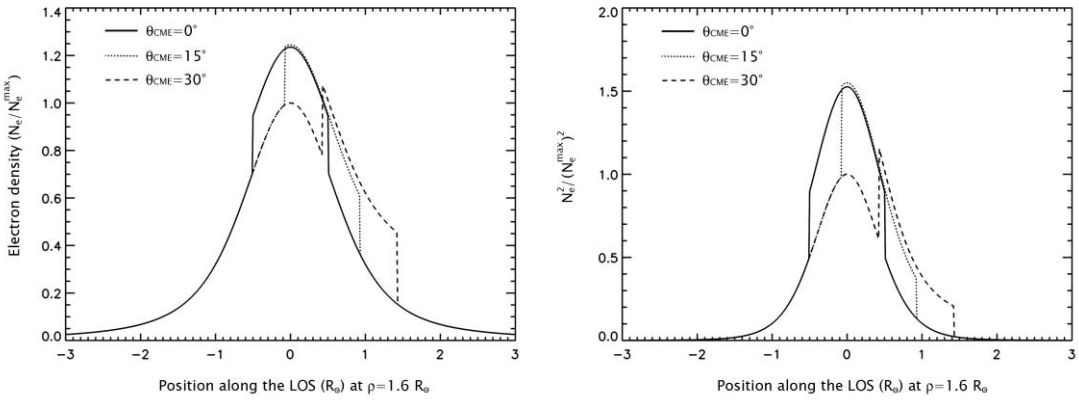

FIG. 13.—*Left*: Typical electron density profiles (normalized to the maximum density value $N_e^{\max}$ on the plane of the sky at the position 0 on the *x*-axis) along the LOS at 1.6 $R_\odot$ computed with the region of additional density (1 $R_\odot$ long) centered on the plane of the sky (*solid line*), and centered at angles $\theta_{\rm CME}$ of 15° (*dotted line*) and 30° (*dashed line*) from this plane. *Right*: Typical squared electron density profiles (line types same as left) used to compute the emission measure (EM) = $\int_{\rm LOS} N_e^2\, dz$; these curves show that the EM value does not significantly change for different $\theta_{\rm CME}$ values.

O VI and Si XII line intensities using the line emissivities given by the CHIANTI spectral code. The oxygen and silicon abundances were taken to have typical coronal streamer values of $\log N({\rm O}) \sim 8.7$ and $\log N({\rm Si}) \sim 7.7$ (see Bemporad et al. 2003). Values in Table 2 show a good agreement (i.e., within the errors of the observed intensities) between the computed and observed O VI and Si XII intensities. Temperatures in Table 2 point toward higher values in the CME structures with respect to the surrounding coronal plasma; in particular, the core region turns out to have a temperature of about 2.8×10^6 K, hence ~76% higher than the 1.6×10^6 K background corona and ~40% higher than the plasma temperature in the CME front. This corresponds to the temperature increase we expected from the observed time evolution of the O VI and Si XII line intensities, as we qualitatively discussed at the beginning of § 5.2.

Before concluding this section we note that, in case the void density is overestimated, the void temperature given in Table 2 should be considered as an upper limit. However, the temperature increase at the CME void and core is further supported by an analysis of the O VI λ1032 line profiles: the kinetic temperatures we derived from the line profile Gaussian fits are on average ~25% larger in the CME void and core regions than in the CME front, as shown in Figure 12; larger temperature variations in the CME regions may be hidden in the average coronal plus CME line profile. The observed line broadening can also be due to the plasma bulk motions along the LOS related to the CME expansion: between 1.6 and 1.9 $R_\odot$ the CME expands by about 30%, and this corresponds to a bulk velocity of ± 50 km s^{-1} along the LOS, hence a Doppler shift of ± 0.17 Å that can possibly explain the observed line broadening; we are unable to distinguish between these two possibilities. Figure 12 also shows that we do not observe significant variations in the average hydrogen kinetic temperature, which keeps nearly constant around 1.6×10^6 K, with slightly larger values at the CME front.

7. CME EVOLUTION BETWEEN 1.6 AND 1.9 $R_\odot$

White-light images show that between 1.6 and 1.9 $R_\odot$ the projected extension of the CME bubble increases by about 30%. Hence, by assuming a CME length L along the LOS of 1.3 $R_\odot$ (i.e., equal to its projected extension) and by using at 1.9 $R_\odot$ the same technique described in § 5.2 to derive the electron density from the observed *pB*, we estimate that both the CME front and core densities increase by ~20%, while the upper limit we derived for the void density is approximately constant.[10] Taking into account the increase in the CME volume it turns out that the total CME mass increased by about a factor of 2.6 (see § 9 for a discussion of this result).

In order to reproduce the observed UV line intensities at this altitude, we derived from the white-light images the plasma outflow speeds that we used to compute the Doppler dimming factors for the Lyα and O VI lines. In particular, the speeds of the CME front, void, and core turn out to be 100, 90, and 80 km s^{-1}, respectively. Unfortunately, fewer exposures were acquired at 1.9 $R_\odot$, and the average UV line intensities are smaller by factors of ~2.6 and 4.4, respectively, for Lyα and O VI λ1032 lines at the CME front. Therefore, the line intensities are affected by larger uncertainties; moreover, at this altitude the transit of the CME core is missed because of a data gap. In any case, by taking larger spatial averages (as already mentioned, the CME projected extension is larger) and by applying the same technique described in § 6, we have been able to derive electron temperatures in the CME front, void, and postcore. The general trend observed at 1.6 $R_\odot$ is also confirmed at 1.9 $R_\odot$; in particular, the observed UV line intensities are well reproduced with a plasma temperature of $10^{6.35}$, $10^{6.45}$, and $10^{6.45}$ K in the CME front, void, and postcore regions (compared to a coronal background temperature of $10^{6.15}$), respectively. Interestingly, these temperatures are slightly higher (by about 10%) than those derived at the lower altitude and suggest a plasma heating during the CME expansion.

As at 1.6 $R_\odot$, we find the O VI λ1032 line profiles observed at 1.9 $R_\odot$ to be broader in the CME void and immediately after the transit of the CME core. However, as we mentioned in § 6, this phenomenon can be due to both the bulk velocity of plasma along the LOS related to the CME expansion and/or a real increase of the kinetic temperatures, and we are unable to distinguish between these two possibilities.

8. UNCERTAINTIES IN THE CME PARAMETERS

In this section we estimate the uncertainties in the plasma density and temperature. In the technique we used to derive densities from the observed *pB* there are two major unknown parameters: the extension L along the LOS of the region with an additional density $\bar{N}_e$ and the position with respect to the plane of the sky,

[10] Between the same altitudes the average background density decreases by about a factor of 2.

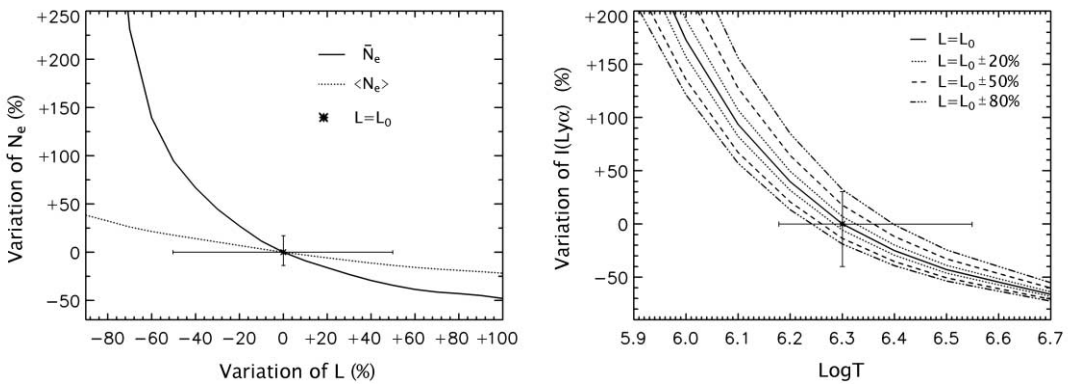

FIG. 14.—*Left*: Computed changes (percent) of the electron density $\langle N_e \rangle$ (*dotted curve*, average background plus CME density along the LOS) and of the additional density $\bar{N}_e$ (*solid curve*) as a function of changes (percent) in the length L along the LOS of the CME region. *Right*: Changes (percent) in the computed Lyα intensity as a function of log T for different values of L (see text).

where this region is centered. All the results we have shown (except for the core mass in spherical geometry) have been derived by assuming $L = 1\ R_\odot$ and $\theta_{\rm CME} = 0$ (where $\theta_{\rm CME}$ is the angle, measured from the plane of the sky, where the region with additional density $\bar{N}_e$ is centered along the LOS); in the following we discuss how changes in L and $\theta_{\rm CME}$ affect the derived parameters.

As we mentioned, the assumption $\theta_{\rm CME} = 0$ is suggested by the lack of significant Doppler shifts in the UVCS Lyα line profiles (i.e., the wavelength shift, if any, is $\leq$0.1 Å, which is the spectral binning of our data). For instance, if we suppose that the region with the enhanced density is centered at angles $\theta_{\rm CME} \leq 30^\circ$ from the plane of the sky, we find an increase in the $\bar{N}_e$-value of less than 28%. The corresponding change in the background plus CME density is smaller, as shown in the left panel of Figure 13: in particular, the $\int_{\rm LOS} N_e\, dz$ and $\int_{\rm LOS} N_e^2\, dz$ change from the value computed with $\theta_{\rm CME} = 0^\circ$ by less than $\sim$3% and 9%, respectively. We conclude that variations in $\theta_{\rm CME}$ do not sensibly affect the computed values of the line intensities (hence the derived temperatures).

The assumption of $L = 1\ R_\odot$ has been suggested by the observed extent (projected onto the plane of the sky) of the CME bubble (see Figs. 7 and 9), which we assumed to be representative also of the CME extent in the direction perpendicular to the plane of the sky. The left panel of Figure 14 shows the variations of the computed electron densities as a function of the assumed length L along the LOS of the region with additional density $\bar{N}_e$. Let us assume, for instance, that with $L = L_0$ we derived a value of $\langle N_e \rangle = \langle N_e \rangle_0$ for the electron density, and that the computed Lyα intensity $I({\rm Ly}\alpha) = I({\rm Ly}\alpha)_0$ reproduces the observed value with log $T = 6.3$ (data points in the two panels of the figure). Hence, the left panel of Figure 14 (*dotted curve*) shows that, by assuming for instance an error of 50% on L (so that $L = L_0 \pm 50\%$), we have $\langle N_e \rangle = \langle N_e \rangle_0 \mp^{15\%}_{20\%}$ (error bars in the left panel of this figure). The corresponding error in the estimate of the Lyα intensity is $I({\rm Ly}\alpha) = I({\rm Ly}\alpha)_0 \pm^{30\%}_{40\%}$ [because $I({\rm Ly}\alpha) \propto L N_e$], and from the right panel of Figure 14 we see that this uncertainty corresponds to log $T = 6.3^{+0.25}_{-0.1}$ on the temperature value (see error bars in Fig. 14, *right*). We note that with this uncertainty all CME temperatures may be either under- or overestimated; hence, temperature differences between different structures will be maintained, and the general trend of higher temperatures at the CME void and core is still valid.

The a priori chosen value of L may significantly affect the derived value of the additional density $\bar{N}_e$ and the computed CME mass. However, as shown by the solid curve of Figure 14 (*left*), changes in the L-value are balanced by changes in $\bar{N}_e$, so that the product $L\bar{N}_e$ keeps approximately constant. As a consequence, larger $\bar{N}_e$-values correspond to smaller values of the volume occupied by the CME (because of the reduced length L along the LOS) and the variation in the computed mass for $L = L_0 \pm 50\%$ are of order only $\pm$5%.

9. DISCUSSION AND CONCLUSION

In this work we studied the early evolution of a CME that occurred on 2000 January 31, with the aim of inferring the structure of the CME in the early stage of its development. Mauna Loa white-light and UVCS UV data allowed us to reconstruct the CME configuration: a comparison of the observed structure with that predicted by the Lin & Forbes (2000) CME model shows the two to be quite similar. In particular, it has been possible to identify, less than 1 hr after the CME initiation, its typical three parts (front, void, and core) in both white-light and UV data.

From the *pB* data we derived the electron densities in these structures: the densities are 35% and $\sim$50% over the average background coronal density for the CME front and core, respectively. From these densities we tentatively derived the mass of different CME structures by assuming some simple geometries for their three-dimensional shape. At 1.6 $R_\odot$ the total mass we compute is $\sim(6\text{–}8) \times 10^{14}$ g. This value is on the small side with respect to more typical CME masses of $\approx 10^{15}$–10^{16} g; however, as pointed out by Lin et al. (2004), the mass of a CME increases with increasing heliocentric distances because of the progressive reconnection of new field lines around the CME bubble. In the Lin et al. scenario, most of the CME mass ($\sim$80%) is added shortly after the onset of reconnection; hence, it is possible that the mass value we derive is representative only of the initial mass of a CME in the early phase of its development. The total mass of this CME (as derived at higher levels from LASCO C3 images)[11] is about 2.1×10^{15} g, hence a factor of $\sim$3 larger than the mass we derive at 1.6 $R_\odot$. The mass of CMEs measured in LASCO images increases with time also because of the partial filling of the telescope field of view and the value of 2.1×10^{15} g derived by LASCO may correspond to the upper limit reached before the CME starts leaving the LASCO field of view. Hence, a CME mass at 1.6 $R_\odot$ of 1/3 its total mass measured at higher levels seems to be realistic. This picture is confirmed by the analysis of data at 1.9 $R_\odot$: taking into account the increase in the CME volume, between 1.6 and 1.9 $R_\odot$ the total CME mass increased by about a factor of 2.6;

[11] See LASCO CME catalog at http://cdaw.gsfc.nasa.gov/CME_list/.

hence, at larger altitude we found a CME mass corresponding to about 90% of its final value.

An interesting result we derived is the temperature variation across different CME structures: in particular, at 1.6 $R_\odot$ we found a temperature higher than the surrounding 1.6×10^6 K corona by factors of 1.23, 1.57, and 1.76 in the CME front, void, and core, respectively. This behavior is confirmed by the analysis of data acquired at 1.9 $R_\odot$ and possibly by the increase (with respect to the external corona) of the oxygen kinetic temperatures observed at both altitudes in the CME void and core. A temperature increase from the CME front toward the core is opposite to that envisaged by the Lin et al. (2004) model, in which plasma in the outer layers of the CME bubble is heated in the CS.

However, laboratory experiments on the free expansion of plasma spheromaks[12] into a vacuum chamber seem to point toward different results. Taylor's relaxation model (Taylor 1974, 1986) predicts that at the end state of a turbulent relaxation process of an isolated plasma, the field, subject to the constraint of conservation of the global magnetic helicity, relaxes to a minimum energy state (often called the "Taylor state"). In particular, in this final equilibrium the plasma is in a force-free state, $\nabla \times \boldsymbol{B} = \lambda \boldsymbol{B}$, with an uniform λ throughout the volume. Experimental studies of Yee & Bellan (2000) demonstrated that during the expansion of a plasma spheromak, while the magnetic helicity K is conserved, the λ-parameter decays with time. Because $\lambda \propto W/K$, where W is the magnetic energy, this implies a magnetic energy dissipation as a result of the expansion. This dissipation leads to a heating of the expanding plasma bubble, which opposes the adiabatic cooling due to the expansion. In particular, "both magnetic heating and adiabatic cooling are expected to occur, but heating will dominate for low-β plasmas" (Yee & Bellan 2000), leading to a total temperature increase in the expanding CME. Hence, our detection of slightly larger temperatures at 1.9 $R_\odot$ confirms this picture. Moreover, because in the Yee & Bellan (2000) experiments the larger λ-decay (hence the larger magnetic energy dissipation) occurs close to the center of the expanding spheromak (see Yee & Bellan 2000; their Fig. 18), we should expect a larger plasma heating (hence larger temperatures) at the center of the expanding bubble, as we observe in our CME.

Interestingly, the same behavior has been predicted by Kumar & Rust (1996), who found that the conservation of magnetic helicity in an expanding flux rope requires a decrease in the total magnetic energy. Magnetic energy transforms into bulk kinetic energy, gravitational potential energy, and heating of the plasma cloud via anomalous resistivity. In the early phases of a cloud's evolution heating dominates over the expansion cooling, and the peak temperature is attained when the flux rope is still within the corona. In this phase the flux rope temperature may increase from $\sim$8000 K up to $\sim 1.7 \times 10^6$ K (see Kumar & Rust 1996). Hence, the event we observed is unique in that, because of the absence of "cool" chromospheric plasma ejected within the CME flux rope, we have been able to study the effect of the CME expansion on plasma temperatures across the CME bubble. In this scenario we may argue that the higher temperature emission observed by Ciaravella et al. (2003) in the CME void and at the top of the prominence core was possibly due to this phenomenon.

A different explanation can be given for the higher (with respect to the coronal background) temperatures observed at the CME front. At the low heliocentric distance of 1.6 $R_\odot$ we are dealing with plasma heating that cannot be provided by a shock, as the speed of the front is too small. The sound speed $v_s = (\gamma p/\rho)^{1/2} = [(5/3)k_B T_e/m_H]^{1/2}$ in the corona at the temperature given above is about 140 km s^{-1}, while the Alfvén speed $v_A = B/(\mu\rho)^{1/2} = B/(8\pi N_e m_H)^{1/2}$ is of order 570 km s^{-1} for a 1 G magnetic field and an electron density of 7.4×10^6 cm^{-3}; hence, the CME front moves at a subsonic and sub-Alfvénic speed. In case of plasma heating by a simple adiabatic compression we expect the product $\Gamma = T_e N^{1-\gamma}{}_e = T_e/N_e^{2/3}$ to be nearly constant. Because $\Gamma_{\rm coronal}/\Gamma_{\rm front} \simeq 0.98$ from the electron density and temperature values given in Table 2 for the CME front and the density and temperature given above for the external corona, we may conclude that, within the uncertainties, plasma heating at the CME front is provided in first approximation by an adiabatic compression. The same result is confirmed, in first approximation, also at 1.9 $R_\odot$.

[12] A plasma spheromak is a toroidal magnetic/plasma configuration in which the magnetic field is generated primarily by plasma currents.

This work initiated during a visit of A. B. to the Harvard-Smithsonian Center for Astrophysics, whose hospitality and support are gratefully acknowledged. A. B. would also like to thank Steve Cranmer and Bernhard Kliem for valuable and useful discussions, and A. L. Stanger for helpful suggestions and for providing the calibrated Mauna Loa data. A. B. and G. P. acknowledge support from ASI-INAF contract I/035/05/0. *SOHO* is a mission of international cooperation between the ESA and NASA.

REFERENCES

Akmal, A., et al. 2001, ApJ, 553, 922
Altschuler, M. D., & Newkirk, G., Jr. 1969, Sol. Phys., 9, 131
Altschuler, M. D., & Perry, R. M. 1972, Sol. Phys., 23, 410
Antonucci, E., et al. 1997, ApJ, 490, L183
Bemporad, A., et al. 2003, ApJ, 593, 1146
———. 2006, ApJ, 638, 1110
Brueckner, G. E., et al. 1995, Sol. Phys., 162, 357
Chanè, E., Jacobs, C., van der Holst, B., Poedts, S., & Kimpe, D. 2005, A&A, 432, 331
Ciaravella, A., et al. 1997, ApJ, 491, L59
———. 1999, ApJ, 510, 1053
———. 2001, ApJ, 557, 351
———. 2002, ApJ, 575, 1116
———. 2003, ApJ, 597, 1118
Delaboudinière, J.-P., et al. 1995, Sol. Phys., 162, 291
Dere, K. P., et al. 1997, Sol. Phys., 175, 601
Elmore, D. F., et al. 2003, Proc. SPIE, 4843, 66
Foley, C. R., Harra, L. K., Matthews, S. A., Culhane, J. L., & Kitai, R. 2003, A&A, 399, 749
Guhathakurta, M., & Holzer, T. E. 1994, ApJ, 426, 782
Ko, Y.-K., et al. 2003, ApJ, 594, 1068
Kohl, J. L., et al. 1995, Sol. Phys., 162, 313
———. 1997, Sol. Phys., 175, 613
Kumar, A., & Rust, D. M. 1996, J. Geophys. Res., 101, 15667
Leamon, R. J., et al. 2004, J. Geophys. Res., 109, A05106
Lin, J., & Forbes, T. G. 2000, J. Geophys. Res., 105, 2375
Lin, J., Raymond, J. C., & van Ballegooijen, A. A. 2004, ApJ, 602, 422
Lin, J., et al. 2005, ApJ, 622, 1251
Liu, Y., et al. 2005, ApJ, 628, 1056
Luhmann, J. G., Li, Y., Zhao, X., & Yashiro, S. 2003, Sol. Phys., 213, 367
Maričić, D., Vršnak, B., Stanger, A. L., & Veronig, A. 2004, Sol. Phys., 225, 337
Mazzotta, P., Mazzitelli, G., Colafrancesco, S., & Vittorio, N. 1998, A&AS, 133, 403
Mickey, D. L., et al. 1996, Sol. Phys., 168, 229
Noci, G., Kohl, J. L., & Withbroe, G. L. 1987, ApJ, 315, 706
Raymond, J. C., et al. 1998, ApJ, 508, 410
———. 2003, ApJ, 597, 1106
Scherrer, P. H., et al. 1995, Sol. Phys., 162, 129

Strachan, L., et al. 2002, ApJ, 571, 1008
Taylor, J. B. 1974, Phys. Rev. Lett., 33, 1139
———. 1986, Rev. Mod. Phys., 58, 741
Tsuneta, S., et al. 1991, Sol. Phys., 136, 37
van de Hulst, H. C. 1950, Bull. Astron. Inst. Netherlands, 11, 135
Ventura, R., Spadaro, D., Uzzo, M., & Suleiman, R. 2002, A&A, 383, 1032
Vourlidas, A., Subramanian, P., Dere, K. P., & Howard, R. A. 2000, ApJ, 534, 456
Vrsnak, B., Maricic, D., Stanger, A. L., & Veronig, A. 2004, Sol. Phys., 225, 355
Webb, D. F., Burkepile, J., Forbes, T. G., & Riley, P. 2003, J. Geophys. Res., 108, 1440
Wilhelm, K., Inhester, B., & Newmark, J. S. 2002, A&A, 382, 328
Yee, J., & Bellan, P. M. 2000, Phys. Plasmas, 7, 3625